RADIO AND X-RAY SIGNATURES OF MAGNETIC RECONNECTION BEHIND AN EJECTED FLUX ROPE

M. PICK,[1] P. DÉMOULIN,[1] S. KRUCKER,[2] O. MALANDRAKI,[3,4] AND D. MAIA[5]

ABSTRACT

We present a detailed study of a complex solar event observed on 2002 June 2. Joint imaging EUV, X-ray, and multiwavelength radio observations allow us to trace the development of the magnetic structure involved in this solar event up to a radial distance of the order of 2 $R_\odot$. The event involves type II, III, and IV bursts. The type IV burst is formed by two sources: a fast-moving one (M) and a "quasi-stationary" one (S). The time coincidence in the flux peaks of these radio sources and the underlying hard X-ray sources implies a causal link. In the first part of our paper we provide a summary of the observations without reference to any coronal mass ejection (CME) model. The experimental results impose strong constraints on the physical processes. In the second part of our paper, we find that a model with an erupting twisted flux rope, with the formation of a current sheet behind, best relates the different observations in a coherent physical evolution (even if there is no direct evidence of the twisted flux rope). Our results show that multiwavelength radio imaging represents a powerful tool to trace the dynamical evolution of the reconnecting current sheet behind ejected flux ropes (in between sources M and S) and over an altitude range not accessible by X-ray observations.

Subject headings: Sun: coronal mass ejections (CMEs) — Sun: radio radiation — Sun: X-rays, gamma rays

1. INTRODUCTION

Sheridan (1970) and Riddle (1970) reported for the first time radio observations at 80 MHz of a "plasmoid" ejected in association with an eruptive solar prominence. In both cases, a moving source appeared soon after a prominence eruption and traveled in the same direction with a constant speed of the order of 200 km s^{-1}. Moreover, in the case studied by Riddle (1970), an underlying stationary source, which could be plausibly interpreted today as radio emission from flare loops, developed later on. These early observations contained some of the ingredients supporting the actual reconnecting models of eruptive events. Since this early period, X-ray observations of solar eruptive phenomena provided an accumulation of results supporting models involving magnetic reconnection. Masuda et al. (1994, 1995) discovered compact impulsive hard X-ray sources above the soft X-ray flare loop in some impulsive limb events. Soft X-ray ejecta were reported in the literature (see references in Ohyama & Shibata 1998). Observations of soft X-ray arcades that form and grow in the aftermath of eruptions were usually interpreted as signatures of magnetic reconnection occurring at progressively greater height. After a new loop is formed by reconnection, the input of heat is mostly stopped. It implies that the hot plasma cools down, and it is observed successively in UV then in optical ranges forming the standard flare loop systems (Svestka et al. 1982; van Driel-Gesztelyi et al. 1997).

All these discoveries led to the development of "standard" models that schematically include two phases: an initial close

and stressed magnetic configuration becomes unstable and erupts; field lines are stretched by the eruption, and a current sheet is formed above the photospheric magnetic inversion line (see, e.g., Lin & Forbes 2000 and references therein). Then, magnetic reconnection occurs along this current sheet: first at low altitudes, then at progressively greater heights (see, e.g., Forbes & Acton 1996). The eruption can be triggered by reconnection above the stressed magnetic configuration as in the breakout model (Antiochos et al. 1999). This model requires a complex magnetic configuration (at least topologically equivalent to a two-dimensional quadrupolar configuration) as well as an increasing magnetic stress in one of the magnetic lobes of the configuration. The region with a growing magnetic stress expands, then builds a current sheet with the overlying oppositely directed stabilizing field. When reconnection starts at a significant rate, the eruption of the underlying stressed field is triggered.

In this paper, we present a detailed study of a complex solar event observed on 2002 June 2. This event was associated with a C8 flare and with an impulsive energetic electron event detected at 1 AU. We analyzed hard X-ray, EUV, and radio imaging data coupled with spectral measurements over a large frequency range. The main characteristic of the radio emission is a broadband continuum modulated by successive packets of fast sporadic bursts. These bursts occur in close time coincidence with hard X-ray peaks (Classen et al. 2003). At metric wavelengths, modulation of broadband continua of long-duration type IV bursts were previously reported by Svestka et al. (1982). They established, for a few events, a close correlation between the modulation observed in hard X-rays and radio. This modulation can occasionally persist over several hours.

In a former study, a similar radio event was detected on 1996 July 9 for which a striking association was found between the flux enhancements and the modifications of the source structure; the topology and evolution of the emitting sources suggested successive magnetic interactions between rising arches and other loops (Pick et al. 1998). Unfortunately, no hard X-ray imaging observations were available at that time.

[1] Observatoire de Paris, LESIA, UMR 8109 (CNRS), 5 Place Jules Janssen, F-92195 Meudon Cedex, France; monique.pick@obspm.fr.

[2] Space Sciences Laboratory, University of California, 7 Gauss Way, Berkeley, CA 94720-7450.

[3] Space Research Laboratory, Democritus University of Thrace, Kondili 9, GR-67100 Xanthi, Greece.

[4] National Observatory of Athens, ISARS, Metaxa and Vas. Pavlou Streets, Penteli, GR-15236 Athens, Greece.

[5] CICGE, Observatório Astronómico Professor Manuel de Barros, Faculdade de Ciências da Universidade do Porto, 4430-146 Vila Nova de Gaia, Portugal.

The main aim of this paper is to analyze in detail a broader set of multiwavelength data for the 2002 June 2 event in order to increase the observational constraints for coronal mass ejection (CME) models. The observations are described in § 2. We leave any physical interpretation in terms of CME models for the next section, so that anyone can confront another type of model to interpret the data. In § 3 we attempt to understand all the available observations within a CME model in the most coherent way. Finally, we conclude in § 4. Results of the data analysis are consistent with the standard models of an erupting twisted flux rope even if the flux rope was not directly observed.

2. DATA ANALYSIS

2.1. *The Observing Instruments*

The multifrequency Nançay Radio Heliograph (NRH; Kerdraon & Delouis 1997) provided images of the radio bursts in the frequency range 432–150 MHz. Spectral data were obtained by the Ondrejov instrument in the frequency range 4200–100 MHz (Jiricka et al. 1993) by the Tremsdorf Observatory of Solar Radioastronomy (OSRA) instrument in the frequency range 800–40 MHz (Mann et al. 1992), by the Nançay Decameter Array (DAM; Lecacheux 2000) in the frequency range 20–70 MHz, and by the Radio and Plasma Wave experiment (WAVES; Bougeret et al. 1995) on board *Wind* below 14 MHz. Furthermore, the high sensitivity of the DAM array allowed us to detect accurately the radio emissions in the high corona and to trace the progression of the event (the DAM is composed of two subarrays, in the opposite sense of circular polarization, having a 4000 m^2 effective aperture each).

The EUV imaging observations were obtained by the Extreme Ultraviolet Imaging Telescope (EIT; Delaboudiniere et al. 1995). The hard X-ray emission was observed by the *RHESSI* mission, which provides imaging spectroscopy from 3 keV to 17 MeV (Lin et al. 2002). No coronal observations in white light were available for this event.

2.2. *Multiwavelength Observations of the Event*

The complex solar event observed on 2002 June 2 was associated with a C8 flare occurring at 10:07 UT inside NOAA AR 9977 (located at S20, W61). This young AR is embedded in a weaker and dispersed field of a previous decayed AR. The closest nearby AR (9965) is located to the northwest of AR 9977, and it had the same global bipolar orientation as the majority of ARs in the southern hemisphere of the associated cycle (negative leading polarity, AR bipole tilted toward the equator).

Radio observations allow us to follow the event in a large coronal altitude range. Figure 1 displays an overview of the spectral radio evolution of the event versus time. Figure 2 shows a comparison between the photon histories measured by *RHESSI*, the flux evolution measured at four frequencies by the NRH, and the spectral evolution measured by OSRA and WAVES. The first weak X-ray event, before 10:10 UT, is associated with a weak radio emission detected above 800 MHz by the Ondrejov radiospectrograph. The event analyzed here coincides with the second strongest X-ray increase. The main results from these radio observations are as follows:

1. The onset of the first groups of type III bursts, visible at decameter to kilometer wavelengths, occurs at 10:13 and 10:15 UT. Some of them are barely detected by the NRH above the flare region located at 0.45 S $R_\odot$, 1.1 W $R_\odot$, then at 0.6 S $R_\odot$, 1.1 W $R_\odot$. They are too weak to be identifiable on the flux versus time
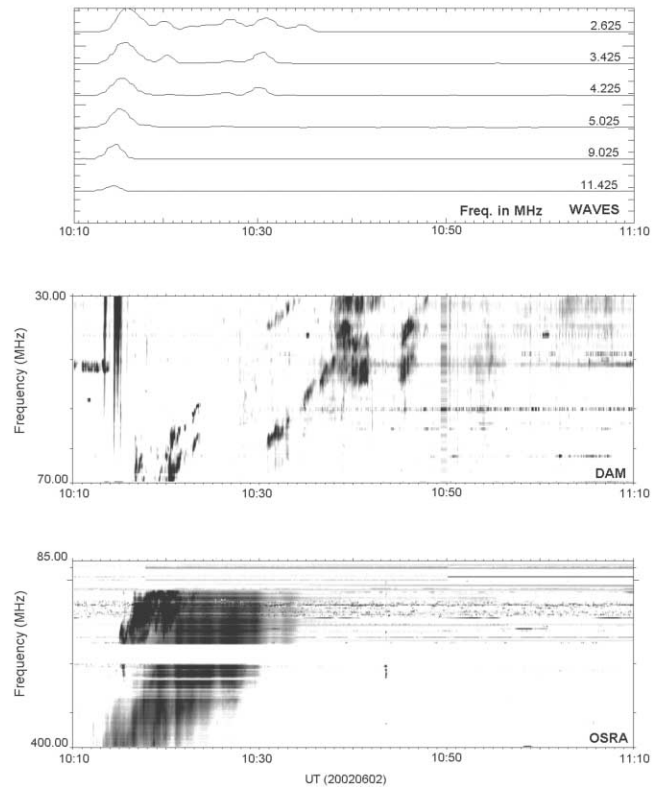

FIG. 1.—Composite including, from top to bottom, a few frequency channels of the RAD2 WAVES spectrograph, the DAM, and the OSRA spectra.

plot at 164 MHz shown in Figure 2. Later on, after 10:25 UT, a few type III bursts are detected at low frequencies by WAVES only, below 5 MHz.

2. This event is associated with an impulsive and anisotropic electron event measured by the Electron, Proton, and Alpha Monitor (EPAM) experiment on board *ACE* (Gold et al. 1998)[6] and by the 3-D Plasma (3DP) experiment on board *WIND* (Lin et al. 2002). We estimated the release time of the electrons detected in the interplanetary medium is 10:26 UT ±2 minutes, i.e., within the time range of the kilometric type III bursts.

3. Following the type III bursts, two successive type II bursts are identified, at approximately 10:16 and 10:20 UT, as measured at 70 MHz. The NRH detected, for the first one, the second harmonic radiation at 164 MHz (not detectable at higher frequencies). The emitting source at this frequency is located at a radial distance of 1.45 $R_\odot$. This altitude corresponds roughly to a density larger by a factor of 2 than the Newkirk density model (Newkirk 1961). We note that these two type II bursts vanish after 10:24 UT and reappear around 10:31 UT. A third type II burst, observed by the DAM, reappears near this time and could be the second harmonic of the first type II burst, although the measured frequency ratio is only 1.6. Measuring the drift in frequency, the speed for the shock depends on the type II considered. The estimated speed is of the order of 370 ± 100 km s^{-1} for the fundamental and 480 ± 100 km s^{-1} for the harmonic (the uncertainty is computed taking a density stratification with a uniform coronal temperature between 1.2 and 1.7 MK). Type II emissions disappear abruptly at 10:38 UT, in coincidence with the onset of a strong period of activity, in the DAM spectrum,
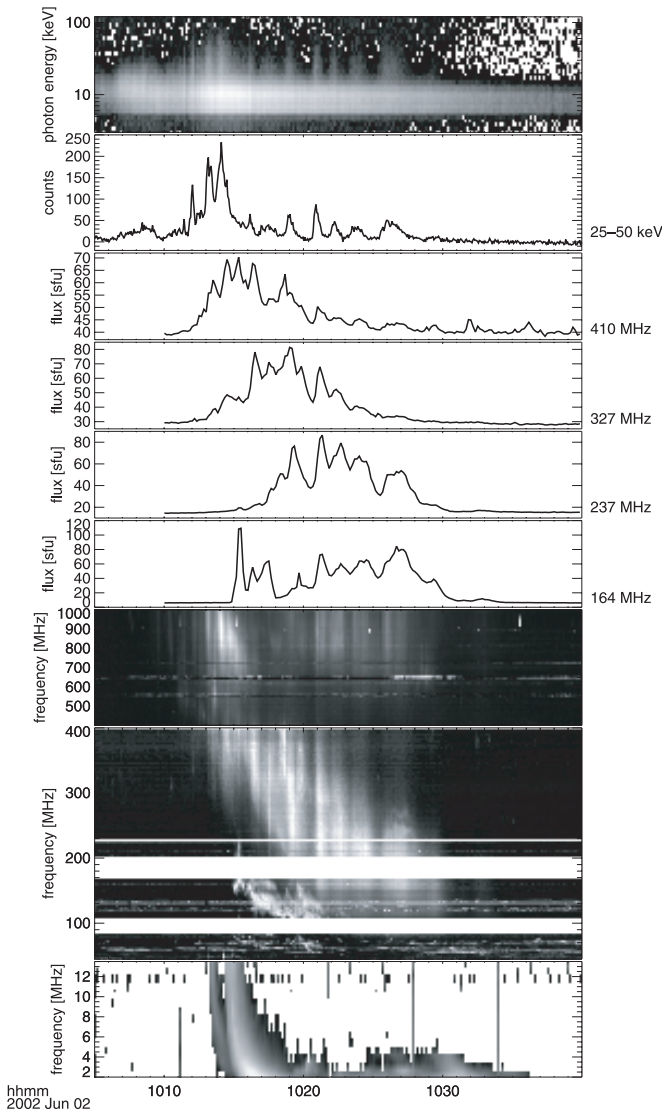

FIG. 2.—Comparison between the photon histories measured by *RHESSI* (*top two panels*), the flux evolution measured at four frequencies by the NRH (*middle four panels*), and the spectral evolution measured by OSRA and by WAVES (*bottom panels*).

lasting for more than 20 minutes and covering a broad frequency range.

    a. The main activity at decimeter-meter range is characterized by a continuum (Fig. 2). The decimeter-meter broadband radio continuum starts to drift to lower frequencies (type IV) at the time when the first group of type III bursts is observed and is strongly modulated over the whole frequency range. This modulation is composed of fast sporadic bursts extending to higher frequencies up to 4 GHz at least (see Fig. 4 in Classen et al. 2003).

    b. Radio emission at decimeter-meter range and the X-ray emission at energies above 20 keV are strongly coupled: both are modulated in phase, and both vanish abruptly at the same time (near the reappearance of the type II emissions at decameter wavelengths; Fig. 1).

The NRH data provide spatial maps of the radio emission in the metric range where the dominant feature is the type IV burst. The detailed data analysis of the NRH data reveals that the radiation arises mostly from the presence of two radio sources (at
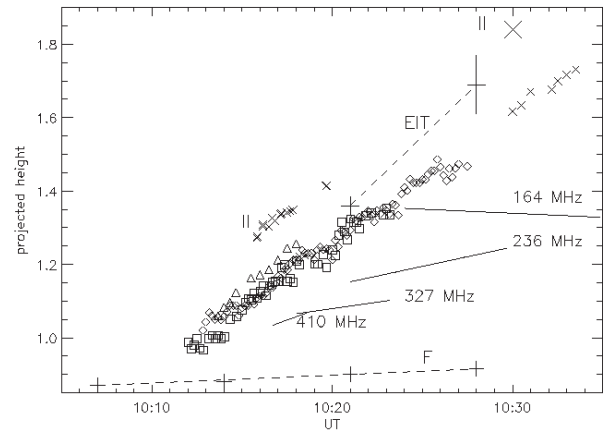

FIG. 3.—Projected positions vs. time of radio sources and main features of the event. The moving source and the quasi-stationary source measured at four frequencies by the NRH are represented by symbols (*triangles*, 410 MHz; *squares*, 327 MHz; *diamonds*, 236 MHz; *small crosses*, 164 MHz) and a linear fit at each frequency (*straight line*), respectively. The moving source has a mean projected speed $\approx 410 \pm 20$ km s^{-1}, while the quasi-stationary sources at each frequency have a smaller drift ($\approx 170 \pm 30$ km s^{-1} at 410 MHz). At 164 MHz, type II bursts (II crosses) are seen at a larger height during a short period (10:16–10:20 UT). The estimated position at 10:30 UT of the type II burst, deduced from DAM and a twofold Newkirk model, is added with a large cross. The drifting radial positions of the EIT leading edge and of the top of the flare loop system (F) are reported with plus signs linked with a dashed straight line.

each frequency). There is not only a moving source (as expected from the type IV burst in Fig. 1) but also, behind it, another source that rises slowly in the corona. A summary of their evolution is given by Figure 3: it displays the projected height versus time for the moving (M) and quasi-stationary (S) sources. A linear fit of the height for the moving source reproduces rather accurately the motion: the projected speed is 410 ± 20 km s^{-1}. The motion of each quasi-stationary source is indicated by a linear fit. These sources appear first at 410 MHz, then at successively lower frequencies, i.e., at successively higher altitudes. Moreover, the moving source appears first for each frequency.

This striking result of two sources is illustrated in Figure 4, which shows images of the sources at 410 MHz. A first source (M) is detected at 10:11 UT, and its rising motion can be followed until 10:18:20 UT. A new stationary source (S) appears at 10:14 UT, behind M, and becomes the dominant one after 10:17:20 UT. At lower frequencies the two sources (M and S) have the same characteristics: they are simply detected higher
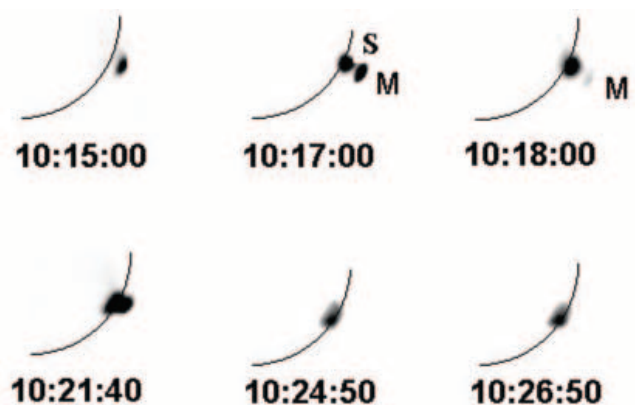

FIG. 4.—Images of the NRH at 410 MHz showing the moving source (M) and the successive quasi-stationary sources (S) appearing at this frequency. The event is close to the solar limb (*curved line*).
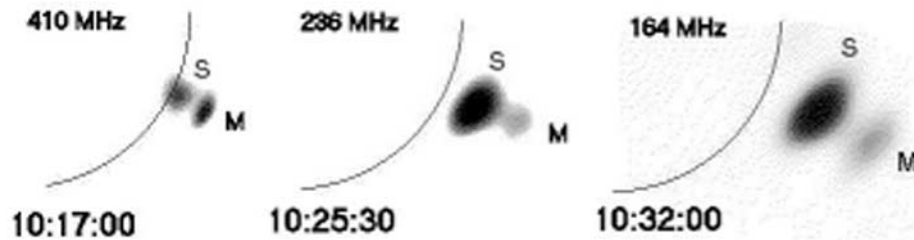
FIG. 5.—Images of the NRH at 410, 236, and 164 MHz, showing the quasi-stationary *sources* (S) and the moving sources (M).

and later (see Figs. 3 and 5); they are also broader because of a larger instrumental lobe.

The M and S sources do not have only a spatial relationship: the time evolution of their flux is related (Fig. 6); the global flux of S is systematically delayed with respect to the global flux of M, and the M and S sources decay with a similar timescale. Moreover, in the period where both sources can be spatially separated by the NRH, the modulation of their fluxes have peaks coinciding in time. This indicates a common origin for these sources.

Polarization measurements, not reported here, show that the S sources are weakly right-hand circularly polarized, of the order of 10%, while M is unpolarized. The quasi-stationary sources lie above a region of dominant negative magnetic polarity. Then, they are likely to be ordinary o-mode emission and are attributed to plasma emission, in agreement with the polarization found for stationary type IV bursts and sources lying above posteruptive loops. The weak degree of polarization is currently observed for limb events. The unpolarized moving source can be attributed either to plasma emission or to gyrosynchrotron emission.

Added to the above general evolution, there are two particularities that we describe below for completeness. At 410 MHz, after 10:21:40 UT, S becomes more complex, extending toward the south, probably showing evidence of the presence of a new source (Fig. 4). This separation has an orientation comparable to the two separating hard X-ray sources observed by *RHESSI* in AR 9977. At 164 MHz, the emission is more complex near the onset of the event with the presence of another moving source distinct from M. It is associated with the type II burst (emission at the harmonic), and it is observed with the NRH during a short period of 10:16–10:20 UT (Fig. 3), in agreement with the OSRA data (Fig. 2).

Three EIT images at 195 Å were available at 10:21, 10:28, and 10:35 UT. The two first images are displayed in Figure 7. The positions of the S and M sources measured at the same times have been reported on the two images and also in Figure 3. These images reveal the presence of an ascending coronal arch (or arch system) with an estimated speed of 540 ± 170 km s^{-1}. This arch expanded not only radially but also laterally. This was more pronounced in the southern part. In the northern part, the arch overlaid the full eruptive active center. The moving M source propagated very closely along the northern edge of the arch. At 10:28 UT this source is located behind the EIT leading edge. The quasi-stationary source is located in the northern foot of the EIT arch, overlying the X-ray sources. The quasi-stationary source at 164 MHz exhibited a lateral displacement that was rather well organized along a direction transverse to the arch, with an apparent projected speed. This displacement accompanied the northern lateral expansion of the EIT arch.

2.3. *Summary of the Data Analysis*

We have made a detailed data analysis of the 2002 June 2 event. Although no coronagraph observations were available for this event, the EIT observations are consistent with the development of a CME. Any interpretation of this event must be consistent with the following characteristics.

1. The presence of a group of type III bursts just at the beginning of the event.

2. The splitting of the type IV burst in two sources: a moving (M, unpolarized) source and a "quasi-stationary" (S, weakly right-hand polarized) source.

3. The appearance of both radio sources (M and S) at successively lower frequencies and at successively higher altitudes.

4. The evolution of the moving radio source at a nearly constant speed (while the emission drifted to lower frequency).
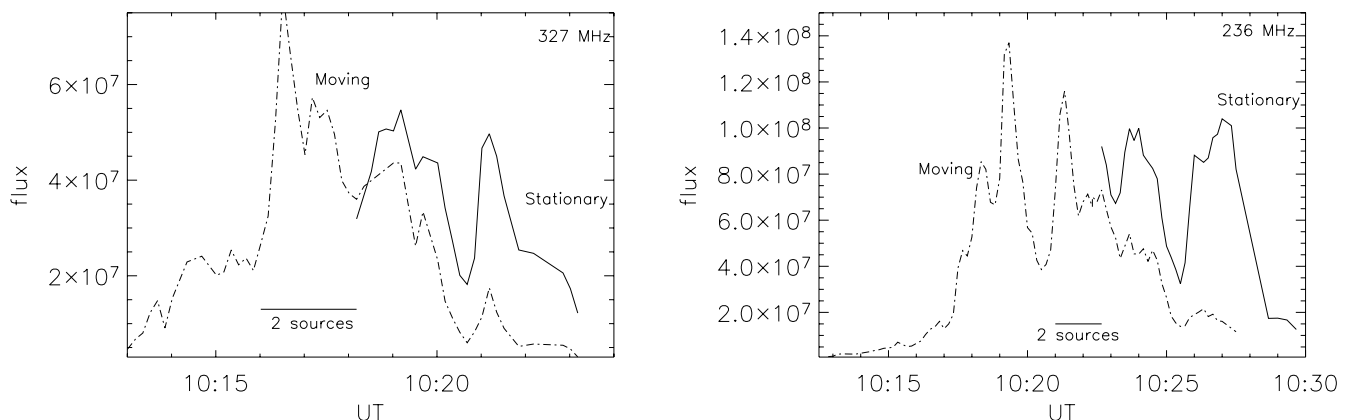

FIG. 6.—Flux evolution at 327 and 236 MHz of the moving (M) and quasi-stationary (S) sources during the time interval when they have significant fluxes. The time period when they are not spatially well separated is denoted by "2 sources."
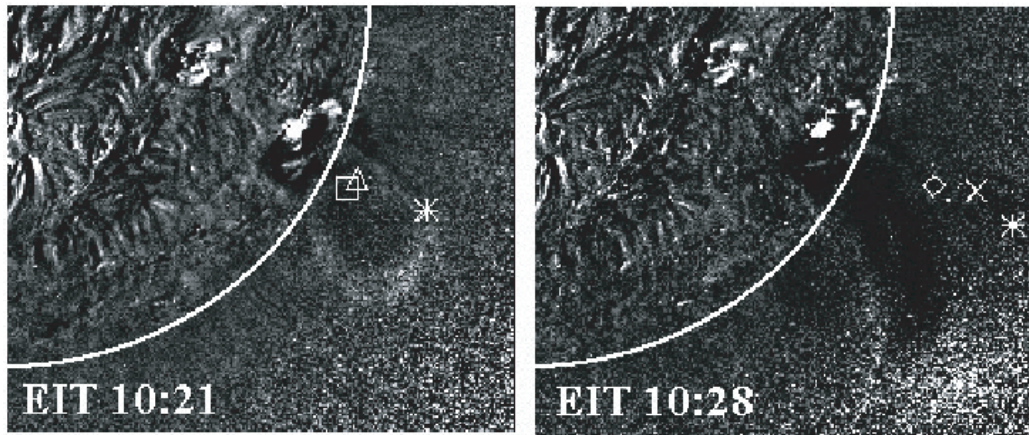
Fɪɢ. 7.—EIT images taken at 10:21 and 10:28 UT. The centroid of the radio sources at the same times are indicated with an asterisk for the moving source (similar positions at different frequencies), with triangles (410 MHz) and squares (327 MHz) on the image at 10:21 UT, and with diamonds (236 MHz) and crosses (164 MHz) on the image at 10:28 UT for the quasi-stationary source.

5. The coincidence of the flux peaks for both the radio sources (M and S) and the hard X-ray sources. It implies that they must be fed by electrons accelerated in the same region. A significant consequence of this correlation is that the moving source cannot be considered as a magnetically detached structure (as an isolated plasmoid), contrary to what was proposed by Classen et al. (2003).

6. The location of these radio sources along the northern edge of an ascending EIT arch overlying the flare and the location of the hard X-ray sources.

7. The evolution of the type II bursts: they are observed during the beginning of the event, then they disappear and reappear later.

8. The coincidence of the reappearance of the type II bursts with the production of type III bursts at low frequencies below 5 MHz and with the estimated release time for the energetic electrons detected at 1 AU. Moreover, near this time, both the type IV burst and the hard X-ray emissions vanished abruptly.

9. Furthermore, considering the respective radial positions of the type II shock, the EIT leading edge, and the radio sources (see Fig. 3), we conclude that both the M and S sources are located behind the shock and the EIT leading edge, when all of them are observed.

3. INTERPRETATION WITHIN A THEORETICAL MODEL

The above set of multiwavelength observations provide an ensemble of constraints to the CME models. On the other hand, many key points are not available with the present observations (e.g., the coronal magnetic configuration). Then the challenge is to link all of these observational facts (§ 2.3) by causal relationships within a theoretical model of CME. We tried several competing models (see, e.g., Klimchuk 2001; Low 2001 for reviews). We end up with a coherent physical interpretation of all these observational facts only with a model having a twisted magnetic flux rope that gets ejected from the Sun. Indeed, such twisted configurations are frequently observed in situ in the interplanetary medium in association with solar CMEs (see, e.g., Lepping et al. 2003 and references therein).

The results of this analysis are summarized below. We start with a short description of the basic two-dimensional model before describing the possible caveats that such simplistic two-dimensional view can bring in interpreting observations (§ 3.1.1). The implications of magnetic reconnection, mainly particle acceleration, are summarized in § 3.1.2. We show the logical re-

lationship between the observational facts within this theoretical framework (§ 3.2). Most of the observational facts are indeed related to the reconnection process located behind the erupting flux rope (§ 3.2.1), while the others are the global consequence of the eruption: the type III and II bursts (§§ 3.2.2 and 3.2.3).

3.1. Summary of the Physical Processes

3.1.1. MHD Model

The simplified key features of the erupting flux rope model are the following (Forbes 1990; Forbes et al. 1994; Mikic & Linker 1994). First, a highly stressed coronal magnetic field gets unstable. Then a twisted flux rope starts ascending upward, stretching the surrounding magnetic field lines. A current sheet forms behind the flux rope, and magnetic reconnection is driven there. A schematic two-dimensional view of this evolution is outlined in Figure 8 (see, e.g., Lin et al. [2004] for a quantitative model of such evolution). A long current sheet is formed at the "two-dimensional X-point" behind the ejected twisted flux rope, since any physically reasonable reconnection rate cannot destroy this current sheet fast enough (Lin & Forbes 2000). With a physically reasonable reconnection rate, indeed even a fairly small rate, the flux rope can be ejected. When the flux rope exceeds typically the local Alfvén speed, a shock is expected to form at its front. This leads to radio emission (type II burst). In the solar context, the erupting magnetic configuration is not isolated but has neighboring magnetic structures, so interaction and magnetic reconnection with the closest ones are also expected during any eruption.

We describe shortly below some of the features not included in the above basic description. First, the two-dimensional representation is mostly done for convenience, but the magnetic structure is indeed fully three-dimensional (see, e.g., Roussev et al. 2003 for a three-dimensional version of the model). Figure 8 is a two-dimensional cut of the three-dimensional configuration across the twisted flux rope. This three-dimensional flux rope is indeed anchored (line-tied) to the photosphere (and not fully detached, as Fig. 8 could falsely give such an impression). Second, the two-dimensional X-point is not necessarily related in three dimensions to a magnetic null point (where the three components of the magnetic field vanish), since a finite magnetic field component perpendicular to the figure is generically present. The separatrices of this two-dimensional configuration are indeed generalized in three dimensions to quasi-separatrix layers, which are thin layers where the magnetic connectivity changes drastically
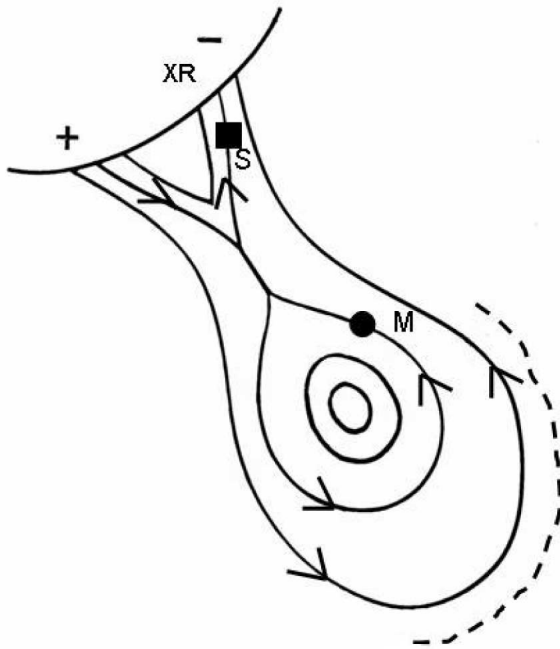
Fig. 8.—Two-dimensional sketch of the magnetic configuration involved in the eruption. A twisted flux rope erupts, driving magnetic reconnection behind it. The particles accelerated in the reconnection region propagate along the reconnected field lines, giving the observed hard X-rays (XR) and the main radio sources (S and M), which correspond to the quasi-stationary sources and moving sources (see § 2.2). A shock is propagating at the front edge of the flux rope (*dashed line*).

(Démoulin et al. 1996). Third, in three-dimensional configurations it is not obvious to identify the twisted flux rope with a low number of turns just by inspecting few field lines (i.e., loops). In most events, the axis of the flux rope is different from the line of sight. It implies that direct evidence of a twisted configuration is expected in rarely observed cases. These few comments on the expected three-dimensional solar erupting configuration show that the two-dimensional geometric features present in Figure 8 (such as a detached flux rope, a well-marked twisted region with an X-point below) should not be taken as observational characteristics of the model.

3.1.2. *Consequences of Magnetic Reconnection*

The main consequences of the magnetic reconnection under the erupting flux rope are the following. Reconnection transforms the overlying arcade-like field lines in two new sets of field lines: a first set of arcade-like field lines located below the reconnection region (flare loops) and a second set of twisted field lines around the flux rope. As reconnection goes on, newly reconnected field lines are added on top of the first set, which then grow in height while individual field lines (loops) relax and shrink (Forbes & Acton 1996). At the same time newly reconnected field lines are added at the border of the erupting flux rope so that its magnetic flux increases. Both this newly added flux and the intrinsic expansion of the rope (because of its higher total pressure than that of the ambient medium) imply a growing size with time.

Three-dimensional magnetic reconnection occurs only if an electric field component parallel to the magnetic field is present (Schindler et al. 1988). Then charged particles are naturally expected to be accelerated in the sites of magnetic reconnection (e.g., Browning & Vekstein 2001; Litvinenko 1996). Other possible acceleration sites are the termination shocks associated to the MHD jets exiting from the reconnection region and colliding with the surrounding fields (e.g., Tsuneta 1995). The present developments of particle acceleration by magnetic reconnection is reviewed by Litvinenko (2003). Whatever is the precise acceleration mechanism, particle beams are predicted in the newly reconnected field lines, thus both above the flare loop system and at the borders of the twisted flux rope.

3.2. *A Synthetic View of Observations within the Model Framework*

Within the above theoretical framework we are now in a position to interpret all the observations of the 2002 June 2 event (§ 2.3). The interpretation of the various emissions is complex, since there are several emitting sources, while some main aspects of the eruption are not observed (e.g., the magnetic configuration).

3.2.1. *Emissions Due to Reconnection behind the Erupting Flux Rope*

In the framework of an erupting flux rope, magnetic reconnection occurs behind the twisted rope (Fig. 8). The accelerated particles form beams along the newly reconnected field lines and propagate both upward and downward. Their signatures are detected with Ondrejov radiospectrograph as packets of fast-drifting emissions. The observed type IV continuum is fed by a part of these accelerated particles that may be trapped on short time periods in the erupting field (e.g., Bruggmann et al. 1994). Electrons are also accelerated repetitively during type IV burst events (e.g., Trottet 1986), as expected within the model of an eruptive flux rope in which reconnection is forced by the evolving configuration.

The particles injected downward at the top of the flare loop system will impact the lower atmosphere forming the hard X-ray emission kernels (thick target process) observed in AR 9977. They will also contribute to the energy input, called "evaporation," which will fill the flare loops observed in soft X-rays and later in EUV. These electron beams will also trigger plasma radio emission, and so they are at the origin of the quasi-stationary source (S). The signature of particles injected upward, at the border of the twisted flux rope, is given only by radio emission (source M). Having this common origin (magnetic reconnection) the hard X-ray emissions, together with the S and M radio emissions, are expected to have a closely correlated evolution, just as is present between the observed multipeaks of emissions (Figs. 2 and 6).

What is the origin of the flux modulation? One possibility is that the reconnection rate is highly time dependent because of the very high Lundquist number of the corona. Alternately, the expected presence of multiple current sheets behind the flux rope (because of the development of MHD turbulence) can also create a highly variable injection rate of energy and accelerated particles (such as a burst each time a current sheet is destroyed).

What is the expected spatial evolution of the radio emissions within the erupting flux rope model (§ 3.1)? The upper radio source forms at the border of the erupting flux rope, so it is expected to follow closely its motion. The lower radio source forms above the flare loop system when the reconnection region has reached the plasma frequency level, and later it is expected to have a slow upward motion, since it is basically the vertical stratification of the corona that determines its height. These expectations, derived from the model, are indeed the main characteristics of the radio sources (M and S) observed with the NRH (see Figs. 3, 4, 5, and 7). At a given observing frequency, the moving source is observed before the stationary source (Fig. 6) simply because there is a lower density in the expanding ejected flux rope than in the lower corona.

In the above model of an erupting flux rope the observed radio sources are formed by particles accelerated in the reconnecting current sheet located below the flux rope. Then, in this model, the positions of the moving and the quasi-stationary radio sources are bracketing the position of the reconnection region. Their spatial distance gives an upper bound to the current sheet length. This distance is relatively small (down to 0.15 $R_\odot$), and it becomes important only at the end of the radio observation period ($\approx$0.3 $R_\odot$; Fig. 3). In their two-dimensional model, Lin & Forbes (2000) found a larger length of the current sheet (typically a factor of 10 larger) for inflow Alfvén Mach numbers M_A of 0.01–0.1, while their magnetic configuration has the typical size of an AR (see their Figs. 6 and 7). What is the origin of this difference: a higher reconnection rate or three-dimensional reconnection works differently than in two dimensions? Only future theoretical developments will permit us to understand this new observational constraint.

The X-ray emissions, and even more so the radio sources, are asymmetric (the radio emission was located mostly in the northern part of the expanding structure; see Fig. 7). What is the origin of this strong asymmetry? First, in observed cases, unlike in most theoretical models, there is no reason to expect any symmetry in the involved magnetic configuration *in* the reconnection process as well as in the accelerated particles. Moreover, even in a symmetric magnetic configuration, the presence of a significant magnetic component along the current sheet is generally present in a three-dimensional sheared configuration. This leads to the separation of accelerated particles with opposite charges in both legs of the reconnected field lines (Zharkova & Gordovskyy 2004). Then, radio and X-ray emissions are generically expected to be asymmetric, as observed.

3.2.2. *Onset of the Event: Type III Bursts*

The analyzed event starts with a group of type III bursts (at 10:13 and 10:16 UT; see Fig. 1). They are classically interpreted as accelerated electrons injected along "open," or at least very extended, field lines. *RHESSI* and EIT data show that AR 9977 is the main origin of the eruption, so the origin of these particles is due to the interaction of the unstable magnetic configuration of AR 9977 with surrounding open field lines.

It is striking that the event starts with a group of type III bursts, since one would rather expect that the erupting flux rope can reconnect more with surrounding open field lines when it is at larger heights, i.e., later in the event. The presence of important current sheets between the AR closed-field configuration and neighboring open field lines before the event is a plausible origin of these early type III bursts: the rapid dissipation of these current sheets would give the energy to accelerate electron beams to form the observed type III bursts. Later on the expanding magnetic configuration still encounters neighboring open field lines, but the energy dissipated in these newly formed current sheets is not large enough to produce significant electron beams. So this approach is a storage-release model, with current sheets formed during the quiet preevent evolution between closed and open field lines. This evolution is comparable with the "magnetic breakout model" of Antiochos et al. (1999) in which the large-scale overlying arcade has being replaced by open field lines. However, it is an open question whether such current sheets can develop or not in the preevent period until the whole magnetic configuration becomes unstable (e.g., by an ideal instability of a flux rope).

3.2.3. *Evolution of the Type II Bursts*

Type II bursts are also observed (Fig. 1). We also analyze them below in the framework of the erupting flux rope model (§ 3.1).

The shock related to the type II bursts is expected to wrap and travel in front of the eruptive configuration. Indeed, the projected position of the type II bursts (10:16–10:20 UT), extrapolated to the observation of EIT at 10:21 UT, lies above the projected position of the EIT leading edge (Fig. 3). Extending this relationship to the full observational interval is difficult, since no imaging of the type II burst is available later (only spectrograph observations are available) and since only one other EIT observation is available (10:28 UT) on which the leading edge has reached the field of view limit. With the drift in frequency of the harmonic, the projected speed of the type II bursts is estimated to be in the interval [380–580] km s^{-1} (§ 2.2). The estimated leading edge velocity, with the only two EIT images available, is [370–710] km s^{-1}. The two velocity ranges overlap, and a lower type II velocity could be due to a radio emission originating from one flank of the CME. Within these uncertainties, we conclude that the type II bursts are consistent with the emission of a shock propagating in front of the CME just as expected in the model.

More surprising, the type II emission disappears after 10:24 UT and reappears after 10:31 UT (Fig. 1). The almost unchanged frequency drift rate shows that the underlying origin of the shock, the erupting flux rope, is not affected. Rather the conditions for the shock emission get temporally changed. The interpretation, supported by the available observations, is that the shock enters a low-density region so that the Alfvén velocity gets much larger than the flux rope velocity. Such lower density region is expected around AR 9977 as follows. Photospheric magnetograms show that AR 9977 is embedded in the remnant field of an earlier AR. In such an old field region, the free magnetic energy is expected to be low. This implies a low coronal heating level and a low plasma density (Démoulin et al. 2003). Part of this large-scale field is also expected to be open, so again with a low plasma density. However, because of the force balance in a low beta plasma, the magnetic field strength in the large-scale bipole should be a continuation of the one present in AR 9977. Then as the shock propagates from the AR field to its surroundings it meets mostly a jump in plasma density, then in Alfvén velocity, which implies that its radio emission disappears.

The revival of the type II emission, at $\approx$10:31 UT, is probably due to the shock entering in a denser structure. The estimated radial altitude of the arch front at that time is approximately 1.8 $R_\odot$. The image of the corona provided by the MK4 coronagraph (June 1, 19:23 UT) indeed shows the presence of a bright streamer, and thus a denser region, at the vicinity of the northern leg of the eruptive arch.

As the flux rope moves up and expands in the corona, it is expected to interact with the surrounding magnetic structures. There is evidence of successive interactions: first, the detection of a few kilometric type III bursts at WAVES below 4 MHz from 10:26 to 10:34 UT; the association with an electron event measured by the EPAM experiment on board *ACE* with an estimated release time of the electrons at 10:26 UT $\pm$2; and finally, the disappearance of the type II (10:38 UT) followed by a sudden onset of an intense and nondrifting broadband emission at decameter wavelengths.

The interaction of the flux rope with the surrounding magnetic structures is expected to build up new current sheets where magnetic reconnection will tend to peal the exterior of the flux rope. It is plausible that this removal of magnetic flux at the border of the flux tube will slow down and even stop reconnection behind the flux rope. Indeed, both X-ray emissions and the type IV burst vanished abruptly at $\approx$10:31 UT, i.e., within the time range of these interactions (Figs. 1 and 2).

4. CONCLUSION

By using a multiwavelength approach covering a wide spectral domain and imaging capabilities in radio, X-rays, and EUV, we were able to (see § 2.3 for a more precise summary)

1. resolve the radio-emitting regions, moving and quasi-stationary (M and S sources), and follow their respective dynamical behavior up to a radial distance of about 2 $R_\odot$;

2. establish a close temporal association between the hard X-rays, and both M and S radio sources; and

3. trace the successive locations of the radio-emitting regions with respect to the ascending arch seen in EUV and to the type II bursts.

These experimental results impose strong constraints on the CME models. Then, in the second step, we found that a model with an eruptive flux rope best relates logically all the above observational facts. In particular the two radio sources (M and S) and the two X-ray sources have a common origin: magnetic reconnection behind the ejected twisted flux rope. Indeed, multiwavelength radio imaging permits us to bracket the reconnecting current sheet behind ejected flux ropes over an altitude range not accessible by X-ray observations.

In light of the present results, we anticipate that some of the radio-moving sources that were described in the literature as isolated structures are not detached structures. This result is coherent with in situ observations, at 1 AU and beyond, of interplanetary magnetic clouds: the detection of regions with counter-streaming electrons indicates that parts of the flux rope are probably still attached to the Sun at both ends (e.g., Richardson 1997; Malandraki et al. 2000).

REFERENCES

Antiochos, S. K., Devore, C. R., & Klimchuk, J. A. 1999, ApJ, 510, 485
Bougeret, J.-L., et al. 1995, Space Sci. Rev., 71, 231
Browning, P. K., & Vekstein, G. E. 2001, J. Geophys. Res., 106, 18677
Bruggmann, G., Vilmer, N., Klein, K.-L., & Kane, S. R. 1994, Sol. Phys., 149, 171
Classen, H. T., Mann, G., Klassen, A., & Aurass, H. 2003, A&A, 409, 309
Delaboudiniere, J.-P., et al. 1995, Sol. Phys., 162, 291
Démoulin, P., Priest, E. R., & Lonie, D. P. 1996, J. Geophys. Res., 101, 7631
Démoulin, P., van Driel-Gesztelyi, L., Mandrini, C. H., Klimchuk, J. A., & Harra, L. 2003, ApJ, 586, 592
Forbes, T. G. 1990, J. Geophys. Res., 95, 11919
Forbes, T. G., & Acton, L. W. 1996, ApJ, 459, 330
Forbes, T. G., Priest, E. R., & Isenberg, P. A. 1994, Sol. Phys., 150, 245
Gold, R. E., et al. 1998, Space Sci. Rev., 86, 541
Jiricka, K., Karlicky, M., Kepka, O., & Tlamicha, A. 1993, Sol. Phys., 147, 203
Kerdraon, A., & Delouis, J. 1997, in Coronal Physics from Radio and Space Observations, ed. G. Trottet (Berlin: Springer), 192
Klimchuk, J. A. 2001, in Space Weather, ed. P. Song, H. J. Singer, & G. L. Siscoe (Geophys. Monogr. 125; Washington, DC: AGU), 143
Lecacheux, A. 2000, in Radio Astronomy at Long Wavelengths, ed. R. G. Stone, K. W. Weiler, M. L. Goldstein, & J.-L. Bougerot (Geophys. Monogr. 119; Washington, DC: AGU), 321
Lepping, R. P., Berdichevsky, D. B., Szabo, A., Arqueros, C., & Lazarus, A. J. 2003, Sol. Phys., 212, 425
Lin, J., & Forbes, T. G. 2000, J. Geophys. Res., 105, 2375
Lin, J., Raymond, J. C., & van Ballegooijen, A. A. 2004, ApJ, 602, 422
Lin, R. P., et al. 2002, Sol. Phys., 210, 3
Litvinenko, Y. E. 1996, ApJ, 462, 997
———. 2003, in Energy Conversion and Particle Acceleration in the Solar Corona, ed. L. Klein (Berlin: Springer), 213
Low, B. C. 2001, J. Geophys. Res., 106, 25141
Malandraki, O., Sarris, E. T., & Trochoutsos, P. 2000, Ann. Geophys., 18, 129
Mann, G., Aurass, H., Voigt, W., & Paschke, J. 1992, in Coronal Streamers, Coronal Loops, and Coronal and Solar Wind Composition, ed. C. Mattok (ESA SP-348; Paris: ESA), 129
Masuda, S., Kosugi, T., Hara, H., Sakao, T., Shibata, K., & Tsuneta, S. 1995, PASJ, 47, 677
Masuda, S., Kosugi, T., Hara, H., Tsuneta, S., & Ogawara, Y. 1994, Nature, 371, 495
Mikic, Z., & Linker, J. A. 1994, ApJ, 430, 898
Newkirk, G., Jr. 1961, ApJ, 133, 983
Ohyama, M., & Shibata, K. 1998, ApJ, 499, 934
Pick, M., et al. 1998, Sol. Phys., 181, 455
Richardson, I. G. 1997, in Coronal Mass Ejections, ed. N. Crooker, J. A. Joselyn, & J. Feynman (Geophys. Monogr. 99; Washington: AGU), 189
Riddle, A. C. 1970, Sol. Phys., 13, 448
Roussev, I. I., et al. 2003, ApJ, 588, L45
Schindler, K., Hesse, M., & Birn, J. 1988, J. Geophys. Res., 93, 5547
Sheridan, K. V. 1970, Proc. Astron. Soc. Australia, 1, 376
Svestka, Z., et al. 1982, Sol. Phys., 80, 143
Trottet, G. 1986, Sol. Phys., 104, 145
Tsuneta, S. 1995, PASJ, 47, 691
van Driel-Gesztelyi, L., et al. 1997, Sol. Phys., 174, 151
Zharkova, V. V., & Gordovskyy, M. 2004, ApJ, 604, 884